Available online at www.sciencedirect.com
ScienceDirect
Trans. Nonferrous Met. Soc. China 34(2024) 2671−2685
Transactions of Nonferrous Metals Society of China
www.tnmsc.cn

CFD modeling of gas−liquid flow phenomenon in lead smelting oxygen-enriched side-blown furnace

Zhen-yu ZHU[1], Ping ZHOU[1], Xing-bang WAN[1], Zhuo CHEN[1], Ling ZHANG[2], Shi-bo KUANG[3]

1. School of Energy Science and Engineering, Central South University, Changsha 410083, China;
2. Changsha Design and Research Institute of Nonferrous Metallurgy, Changsha 410019, China;
3. ARC Research Hub for Computational Particle Technology, Department of Chemical Engineering, Monash University, Wellington Rd, Clayton, VIC 3800, Australia

Received 4 April 2023; accepted 8 November 2023

Abstract: A validated numerical model was established to simulate gas−liquid flow behaviors in the oxygen-enriched side-blown bath furnace. This model included the slip velocity between phases and the gas thermal expansion effect. Its modeling results were verified with theoretical correlations and experiments, and the nozzle-eroded states in practice were also involved in the analysis. Through comparison, it is confirmed that the thermal expansion effect influences the flow pattern significantly, which may lead to the backward motion of airflow and create a potential risk to production safety. Consequently, the influences of air injection velocity and furnace width on airflow behavior were investigated to provide operating and design guidance. It is found that the thin layer melt, which avoids high-rate oxygen airflow eroding nozzles, shrinks as the injection velocity increases, but safety can be guaranteed when the velocity ranges from 175 to 275 m/s. Moreover, the isoline patterns and heights of thin layers change slightly when the furnace width increases from 2.2 to 2.8 m, indicating that the furnace width shows a limited influence on production safety.

Key words: multiphase flow; horizontal gas injection; backward motion of airflow; gas thermal expansion; side-blown furnace; lead smelting

1 Introduction

Increasing demand for metals and depletion of high-grade ores have prompted intensive investigations on more efficient technologies and devices to extract metals [1,2]. Bath smelting technologies for lead and copper production have been used more frequently due to the higher compatibility to deal with complex secondary resources such as e-waste, and Pb-battery [3−6]. Upgraded from the Vanyukov copper smelting furnace, the lead smelting oxygen-enriched side-blown bath furnace (OSBF) has been newly designed and successfully implemented in China. This lead smelting OSBF is able to oxidize not only the lead concentrate but also the lead paste, which is the main recycled content in scrapped Pb batteries. Apart from the recycling feature, the OSBF is also characterized by the low operating cost, high oxygen utilization rate, high level of automation, and high airtightness. Also, its concise structure and nozzle arrangement create large potential in increasing its capacity. All these advantages promote its further environment-friendly development.

For bath smelting furnaces, the gas−liquid flow in a high-temperature bath is essential for the interaction between molten slag and oxygen airflow [7]. The nozzles of the OSBF are installed in

Corresponding author: Zhuo CHEN, Tel: +86-13974891750, E-mail: chenzhuo@csu.edu.cn
DOI: 10.1016/S1003-6326(24)66568-4

the slag layer so that it is able to stir the slag with high efficiency while not disturbing the settling of molten metal. This flow characteristic is shared with other classical side-blown furnaces, such as the Vanyukov furnace [8,9], the P-S converter [10−13], and the fuming furnace [14,15]. However, as the lead slag has a higher density and viscosity, a unique gas−liquid flow feature may appear and cause severe problems during the practice of OSBF. For example, the high-rate oxygen airflow may be easier to move backward after leaving the nozzles and staying around them. This phenomenon could cause the nozzles to be eroded soon, especially under such a high temperature. Once the nozzles were eroded entirely, the molten slag would spill over the plant and create a severe accident. Thus, it is of significance to fully understand the inner airflow behavior in the high-temperature bath of the OSBF so that the life circle of the smelter can be prolonged.

To reveal the flow phenomena of horizontal gas injection in the side-blown furnace, previous experimental research contributes a fundamental understanding of the airflow trajectory, penetration depth, and half-value radius [16,17]. LIU et al [18] and XIAO et al [19] established the cold-state similarity model of a side-blown furnace and explored the operating impacts on fluid fluctuation height, airflow penetration depth, and the circulation mixing zone. However, the backward motion of airflow in the horizontal injection or side-blown furnaces has rarely been investigated in recent years. THEMELIS [20] deduced the theoretical trajectory equation of horizontal jet airflow and connected the flow pattern with the modified Froude number. Then, the initial angle of airflow was found to expand when the liquid density and viscosity increased [21]. Also, the backward motion was confirmed when blowing the molten metal [22]. Even though BUSTOS et al [23] found that the freezing accretion could guide the airflow pattern and protect the nozzles to some extent, the risk of severe corrosion caused by airflow still exists in such a high-temperature bath, especially when interacting with high-viscosity lead slag in the OSBF.

Due to the typical characteristics of high temperatures and harsh conditions in smelting processes, obtaining information directly from the furnace or conducting precise industrial experiments is difficult. As an alternative method, the CFD modeling is a powerful tool for better understanding the hydraulic phenomena inside the large-scale furnaces [24−27], especially the flow and interactions of the gaseous and metallic phases [28−30]. Consequently, the corresponding optimization can be determined. The horizontal gas injection behaviors in different side-blown furnaces have been widely investigated [31−33], which provide various choices of numerical models. Different CFD multiphase models focus on different gas−liquid flow phenomena and may obtain inconsistent results. ZHANG et al [9] used the VOF model to simulate the Vanyukov furnace, and the result showed that the airflow moved backward and attached to the wall. In contrast, LIU [34] obtained a different flow behavior in the same furnace by using the Mixture model. Since the numerical models have their unique features, establishing a suitable model is essential to investigate the lead smelting OSBF. Moreover, as the highly expanded airflow might influence the flow pattern [35], the gas thermal expansion effect should be fully considered in such a high-temperature circumstance. With such a valid numerical model to simulate the hot-state lead smelting OSBF, airflow behaviors such as the backward movement can be investigated, and further optimization of operation and structure can be made as well.

In this work, a numerical study of the flow behaviors in the OSBF using the CFD approach was presented. It aims to establish better numerical modeling of the lead smelting OSBF, consequently investigating the impacts of the backward motion. To achieve this goal, two different homogeneous multiphase models are used to perform numerical simulations. The results are examined in terms of airflow trajectory, half-value radius, and penetration depth. Then, the model that can better predict the experimental measurements is selected. The selected model including air thermal expansion is used to investigate the airflow backward behavior in a high-temperature OSBF. Note that the airflow velocity and furnace width are essential to optimize the operating mode and design of OSBF, the effects of these two key variables on the nozzle erosion are particularly quantified to improve the furnace campaign life. The findings should be useful to confirm the multiphase model's applicability in

simulating the hot-state OSBF, and to better understand the complex flow behaviors of gas and lead slag.

2 Simulation method

As typical representatives of the homogeneous multiphase models, the VOF and Mixture models are commonly used in the study of horizontal submerged gas injection, but they have different characteristics. The Mixture model treats the multiphase as the inter-penetrating continua, and it includes the slip velocity between phases to deal with the large velocity difference. By contrast, the penetration and slip velocity are not fully considered in the VOF model, but the clear interface between the phases can be captured. Therefore, comparisons should be made first to establish a suitable model for the CFD modeling of OSBF.

2.1 Governing equations for multiphase models

The numerical models have been reported in other literature [28,36], thus only outlined here for brevity. The governing equations of the VOF and Mixture models include the mass, momentum, and energy conservations, which are shown in Table 1, where α is the volume fraction, ρ is the density, and $\boldsymbol{v}$ is the velocity vector. In the momentum equation, p is the pressure, $\boldsymbol{g}$ is the gravity vector, μ is the viscosity, and $\boldsymbol{F}$ is the body force. In the energy equation, E is the energy, k_{eff} is the effective thermal conductivity, and T is the temperature. The subscripts in the three governing equations are summarized: q denotes the qth phase, m is the mixture of all phases, k is the secondary phase, and p is the particle phase. In addition, the $\boldsymbol{v}_{\text{dr},k}$ denotes the drift velocity, τ is the relaxation time, f_{drag} is the drag force taken from SCHILLER [37], and $\boldsymbol{a}$ is the secondary phase particle's acceleration. The realizable k–ε model is selected as the turbulence model according to the literature [18]. In addition, as the Mixture model can introduce the slip velocity, the algebraic slip formulation proposed by MANNINEN et al [38] is used in this work.

2.2 Thermal expansion

In the former side-blown modeling, the effect of high temperature on gas density is usually simplified by setting the gaseous property as a constant [9]. This simplification works reasonably in the simulation of hydraulic experiments because the gas and liquid are both at the ambient temperature (normally 300 K). However, the molten slag in the smelting bath is usually over 1200 K, while the injected gas is 300 K. This large temperature difference would cause an over three-time expansion in airflow volume. ORYALL and BRIMACOMBE [35] found that the initial expansion angle of airflow would increase to 150°−155° in the 293 K gas−metal system. This angle would be much larger when the temperature difference increases, which creates a significant impact on flow pattern. Thus, the thermal expansion

Table 1 Governing equations of mathematical model

Model	Remark	Equation
VOF	Mass	$\frac{\partial}{\partial t}(\alpha_{\text{q}}\rho_{\text{q}})+\nabla\cdot(\alpha_{\text{q}}\rho_{\text{q}}\boldsymbol{v}_{\text{q}})=0$
	Momentum	$\frac{\partial}{\partial t}(\rho\boldsymbol{v})+\nabla\cdot(\rho\boldsymbol{v}\boldsymbol{v})=-\nabla p+\nabla[\mu(\nabla\boldsymbol{v}+\nabla\boldsymbol{v}^{\text{T}})]+\rho\boldsymbol{g}+\boldsymbol{F}$
	Energy	$\frac{\partial}{\partial t}(\rho E)+\nabla\cdot[\boldsymbol{v}(\rho E+p)]=\nabla\cdot(k_{\text{eff}}\nabla T)$
Mixture	Mass	$\frac{\partial}{\partial t}(\rho_{\text{m}})+\nabla\cdot(\rho_{\text{m}}\boldsymbol{v}_{\text{m}})=0$
	Momentum	$\frac{\partial}{\partial t}(\rho_{\text{m}}\boldsymbol{v}_{\text{m}})+\nabla\cdot(\rho_{\text{m}}\boldsymbol{v}_{\text{m}}\boldsymbol{v}_{\text{m}})=-\nabla p+\nabla\cdot[\mu_{\text{m}}(\nabla\boldsymbol{v}_{\text{m}}+\nabla\boldsymbol{v}_{\text{m}}^{\text{T}})]+\rho_{\text{m}}\boldsymbol{g}+\boldsymbol{F}+\nabla\cdot\left(\sum_{k=1}^{n}\alpha_k\rho_k\boldsymbol{v}_{\text{dr},k}\boldsymbol{v}_{\text{dr},k}\right)$
	Energy	$\frac{\partial}{\partial t}\sum_{k=1}^{n}(\alpha_k\rho_k E_k)+\nabla\cdot\sum_{k=1}^{n}[\alpha_k\boldsymbol{v}_k(\rho_k E_k+p)]=\nabla\cdot(k_{\text{eff}}\nabla T)$
	Slip velocity	$\boldsymbol{v}_{\text{pq}}=\frac{\tau_{\text{p}}}{f_{\text{drag}}}\frac{(\rho_{\text{p}}-\rho_{\text{m}})}{\rho_{\text{p}}}\boldsymbol{a}$

of airflow is considered in all simulations of the gas−slag system in this study to describe the flow field more precisely. The equation of gas density is expressed as

$$\rho_g = p_{op} M_w / (RT) \quad (1)$$

where ρ_g is the gas density, p_{op} is the operating pressure, R is the universal gas constant, and M_w is the relative molecular mass.

2.3 Geometries and boundary conditions

To analyze the applicability of numerical models, simulations were carried out with two models to study the horizontal submerged gas injection in both the experimental hydraulic apparatus and an industrial oxygen-enriched side-blown furnace. By involving two geometries in different scales and conditions, on the one hand, it is to compare the numerical and theoretical results, helping to understand the applicability under the hydraulic experimental condition. On the other hand, it is to reveal the thermal effect on the two-phase flow by considering the temperature difference in the industrial furnace.

The geometry of the hydraulic model used in the numerical simulations is shown in Figs. 1(a) and (b). The detail of the experimental apparatus can be found in our previous work [18] which established a 1:5 scaled model of lead smelting OSBF. The mass flow inlet is used to keep in line with the modeling of OSBF because the air density will change with temperature. Meanwhile, the periodic boundary is also applied to eliminating the impact of walls on the airflow pattern.

The basic structure of an oxygen-enriched side-blown furnace has been given and introduced in Ref. [39]. Since thirteen pairs of nozzles are arranged in a staggered pattern along both sides of the furnace, simplification was made by selecting a slice including four pairs of nozzles like the previous method in Ref. [39], which is shown in Figs. 1(c) and (d). In this study, four pairs of nozzles are included in the geometry, but only the two pairs of nozzles in the middle are used for data analysis to eliminate the influence caused by the wall boundary. Also, it should be noted that only one nozzle on each side is opened to achieve staggered blowing according to the operating mode in the metallurgical plant.

The structures and operating parameters are listed in Table 2 and values in parentheses are used in the following parametric study. In the simulation of the hydraulic model, the object is a gas−water system, and the liquid properties are the common

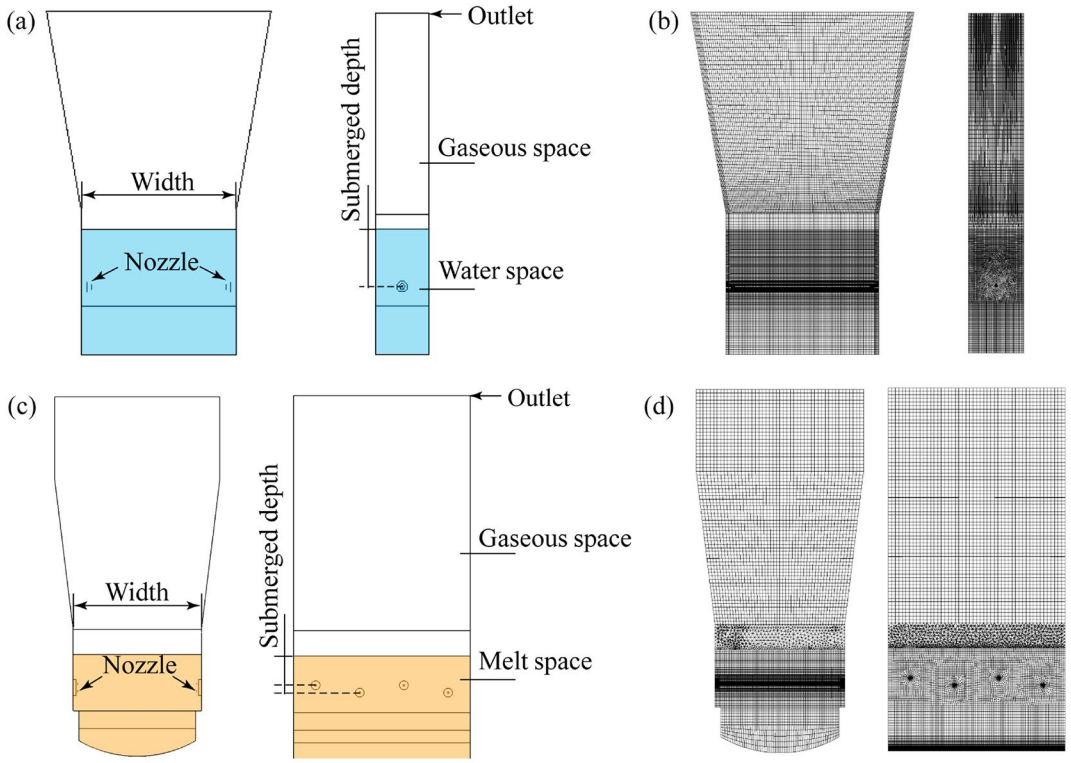

Fig. 1 Schematic of computational domains (a, c) and mesh (b, d) used in simulation: (a, b) Hydraulic model; (c, d) OSBF

Table 2 Parameters used in simulations

Object	Type	Parameter	Value
Hydraulic model	Structure	Nozzle diameter/m	0.004
		Nozzle submerged depth/m	0.15
		Model width/m	0.40
	Gaseous phase	Air mass flow rate/(kg·s^{-1})	1.205
		Air velocity/(m·s^{-1})	100
		Air temperature/K	298
OSBF	Structure	Nozzle diameter/m	0.032
		Nozzle submerged depth/m	0.500/0.625
		Model width/m	2.2 (2.5/2.8)
	Gaseous phase	Air mass flow rate/(kg·s^{-1})	0.218 (0.170/0.266)
		Air velocity/(m·s^{-1})	225 (175/275)
		Air temperature/K	298
	Slag phase	Slag temperature/K	1473
		Slag density/(kg·m^{-3})	4478
		Specific heat capacity/(J·kg^{-1}·K^{-1})	443
		Viscosity/(Pa·s)	0.605

water parameters under 298 K. In the OSBF simulation, two melt phases are simplified into one slag phase, as the thin lead layer at the bottom would not influence the result in this study but could slow down the computation. The slag density and specific heat are calculated according to their mineralogical components, and the viscosity is determined according to Ref. [40].

The computations were all performed on the 4 × Intel Xeon Gold 6248 (80 cores) platform. Before starting the numerical research, the mesh independence test was performed using the hydraulic model, and the comparative data are shown in Table 3. The numerical results of three different meshes were compared with the airflow penetration depth in Ref. [18]. Based on the accuracy and computational time, Mesh 2 was selected to be used in the following study, as shown in Fig. 1(b).

Regarding the Mixture model, the diameter setting of the disperse phase can influence the result, which refers to the gaseous phase in our study. However, limited by the complexity of the side-blown two-phase flow, relative experimental data are rare in current literature. Therefore, cases with bubble diameters of 2, 1, 0.4, 0.04 and 0.004 mm were all examined under the simulation of the gas−water system. It is found that the dispersion of the gaseous phase will be limited as the bubble diameters increase. However, the difference is no longer significant when the bubble diameter is smaller than 0.4 mm. Thus, the diameter of 0.4 mm is selected in the following study after comparing it with the observed phenomenon in Ref. [18]. The corresponding diameter used in the simulation of large-scale OSBF is scaled up according to the geometric similarity ratio, which is 3.2 mm.

Table 3 Mesh independence test for geometry model

Mesh No.	Mesh size around nozzle/mm	Mesh size in liquid zone/mm	Error to experiment/ %	Total time/h
1	0.67	1	3.82	29.9
2	0.67	2	7.83	18.3
3	0.67	4	13.33	10.3

3 Results and analysis

3.1 Comparison and validation of numerical results

The hydraulic experiment is commonly used to investigate the flow characteristics in large-scale furnaces, and it also helps to establish many mathematic correlations, which are convenient for the validation of numerical results. In this part, the multiphase flow characteristics in the cold-state hydraulic model and the hot-state industrial furnace were analyzed and compared to determine the suitable model.

3.1.1 Brief review of conventional description

Conventional descriptions used to analyze the horizontal submerged gas injection commonly include the flow trajectory, the airflow half-value radius, and the penetration depth. Therefore, classical theory and experimental correlations referred to in this study are briefly reviewed, and the schema of horizontal airflow is given in Fig. 2 for the convenience of illustration.

(1) Flow trajectory

The airflow trajectory is one of the most significant indices to evaluate the flow characteristic. Based on the mass and momentum conservation,

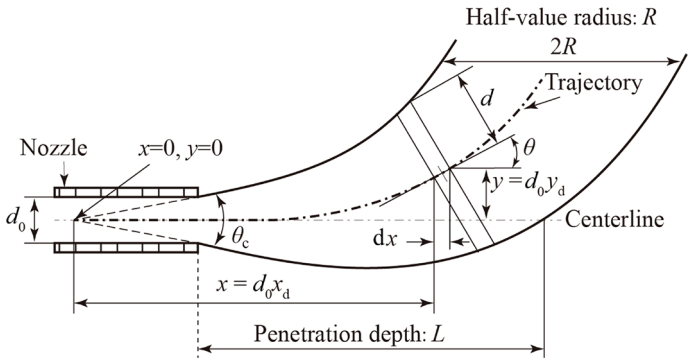

Fig. 2 Schematic of horizontal submerged gas injection (adapted from Ref. [20])

THEMELIS [20] derived the generalized dimensionless Eq. (2) to describe the airflow trajectory of horizontal airflow injection in the air−water system. Based on this, ZHU et al [41] modified the volume fraction and derived the equation for the air−metal system. In this study, Eq. (2) was used to obtain the flow trajectory through the Runge−Kutta method, which is also employed in Ref. [42].

$$\frac{\mathrm{d}^2 y_\mathrm{d}}{\mathrm{d}x_\mathrm{d}^2}=4\left(Fr'\right)^{-1}\left[\frac{\tan^2\left(\theta_\mathrm{c}/2\right)}{\cos\theta_0}\right]\left[1+\left(\frac{\mathrm{d}y_\mathrm{d}}{\mathrm{d}x_\mathrm{d}}\right)^2\right]^{1/2}x_\mathrm{d}^2 C \tag{2}$$

where x_d and y_d denote the dimensionless width and height, respectively, Fr' is the modified Froude number, θ_c is the initial angle of airflow, θ_0 is the nozzle angle, and C is the volume fraction.

(2) Half-value radius

The correlation of the half-value radius is first proposed in the bottom injection by CASTILLEJOS and BRIMACOMBE [16]. Then, ZHU et al [17] applied it to the horizontal injection and verified it with experimental data by modifying the coefficient. The half-value radius shown in Fig. 2 is determined from the cross-section of airflow, which is assumed to be a circle. The correlation is described in Eq. (3), which has been verified and proved to agree well with the experimental results in the air horizontal injection [17].

$$R\left(\frac{g}{Q_0^2}\right)^{1/5}=0.479\left(\left(\frac{gd_0^5\left(\rho_\mathrm{l}-\rho_\mathrm{g}\right)}{Q_0^2\rho_\mathrm{g}}\right)^{0.184}\left(\frac{y}{d_0}\right)^{0.48}\right) \tag{3}$$

where R is the half-value radius, Q_0 is the volume flow rate, d_0 is the nozzle diameter, and ρ_g and ρ_l are the gaseous and liquid densities, respectively.

(3) Penetration depth

HOEFELE and BRIMACOMBE [21] conducted an empirical equation for the air horizontal injection, linking the dimensionless depth with Fr' and gas-to-liquid density ratio, as described in Eq. (4). The penetration depth (L) is defined as the length from the tuyere tip to the intersection between the centerline and the outer line of airflow, as shown in Fig. 2.

$$L/d_0=10.7(Fr')^{0.46}(\rho_\mathrm{l}/\rho_\mathrm{g})^{0.35} \tag{4}$$

3.1.2 Flow characteristics in gas−water system

In the unsteady flow simulation, the time that it takes for the multiphase flow to reach a relatively steady state should be determined first. Thus, the liquid zone was selected to compute the volume-weighted mean velocity, as shown in Fig. 3. It can be seen that the mean velocity increases rapidly in the time duration of 0−0.5 s and tends to be steady with slight fluctuation after 0.5 s. Therefore, the two-phase flow is considered to reach a steady state after 0.5 s, and this steady stage is used for further analysis.

As the flow reaches the steady state after 0.5 s, the contours of air volume fraction at t=1 s are

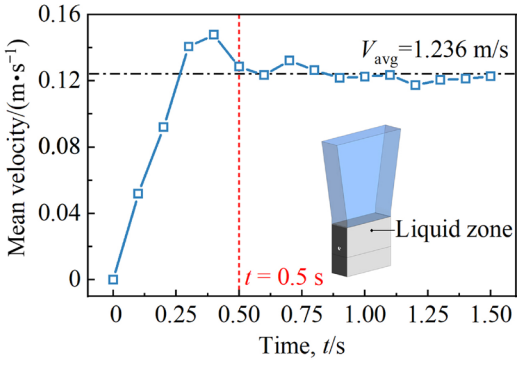

Fig. 3 Mean velocity in liquid zone

shown in Figs. 4(b) and (c) to make a comparison with the experimental result in Ref. [18]. In the experimental result (Fig. 4(d)), the outlines of the gas jet are sketched out with black lines, and numerous tiny bubbles can be found dispersing inside the jet. In comparison, small bubbles can also be found in the simulation results, but the bubble quantities are much less than those in the experimental photo. This is considered to be a result of two aspects. On the one hand, the experiment used six pairs of nozzles for air injection. Hence, the bubbles seen in the photo are actually a superimposition of all the bubbles along the length direction. On the other hand, the bubbles caught in the simulation greatly depend on the mesh sizes. It means that bubbles smaller than the grids cannot be captured with the VOF model. Figure 4(c) is the simulation result with the Mixture model. As the Mixture model allows the phases to penetrate into each other, a clear interface cannot be obtained. In other words, tiny bubbles should be dispersed in the area where the air volume fraction is between 0 and 1, but they cannot be clearly distinguished in the result.

To make a further comparison, the simulation results during 0.5−1.5 s were used to get the average values, so that the accidental error by taking data at one specific moment can be avoided. With the aim of this, the image binarization process is used to post-process the contours of the air volume fraction, as shown in Fig. 5. The RGB contours are transferred into grayscale images, and then the average result could be obtained by overlaying all the images. Figure 5 shows the example of the Mixture model result, and the same process is applied to the result of the VOF model. Through the final binary images, it is easy to get further data such as the flow trajectory, half-value radius, and penetration depth.

The jet flow trajectory equations proposed by THEMELIS et al [20] are introduced to make comparisons with the numerical results, as shown in Fig. 6. The dimensionless width and height used here have been illustrated in Fig. 2. The dots represent the mean values of numerical results, and the error bars show the largest deviations. As shown in Fig. 6, the flow trajectory is more similar to the Themelis's theoretical result when using the Mixture model. The flow trajectory of the VOF only approaches the theoretical result when the x_d is less than 10, and it goes directly upward after that. According to the numerical governing equations, the main reason causing these differences is considered to be the slip velocity introduced in the Mixture model, leading the airflow reserve more momentum in the horizontal direction.

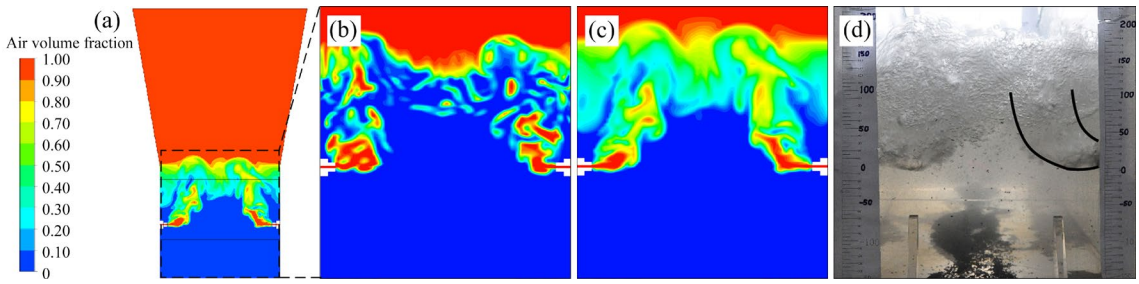

Fig. 4 Snapshots of air volume fraction: (a) Original example; (b) VOF; (c) Mixture; (d) Experiment

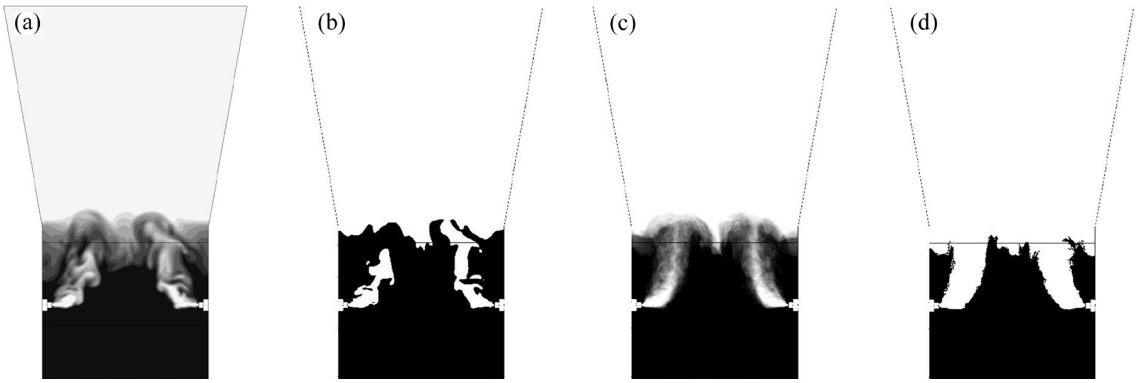

Fig. 5 Image binarization process: (a) Grayscale; (b) Binary; (c) Average; (d) Final binary

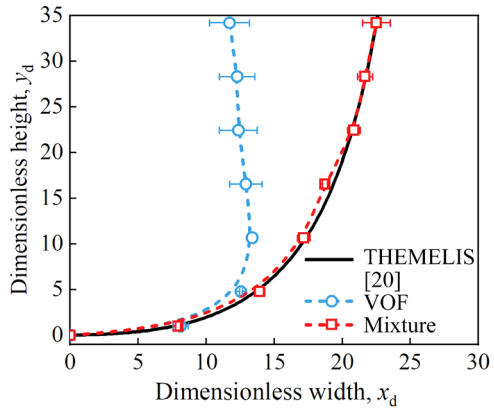

Fig. 6 Comparison of airflow trajectory

The computational curves of the correlation of ZHU et al [17] and the numerical results are shown in Fig. 7. It can be seen that the result of the VOF model shows a significant difference from the correlation curves, especially when $25 < y < 75$. For the Mixture model, the numerical result matches better with correlation curves. This means that using the Mixture model can obtain better results of the half-value radius than the VOF model.

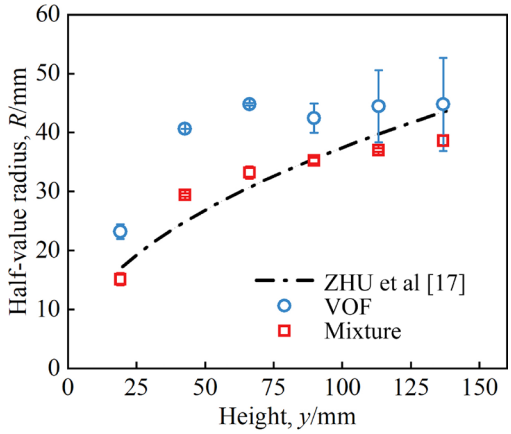

Fig. 7 Comparison of half-value radius

The penetration depths computed from correlation of HOEFELE and BRIMACOMBE [21] are listed in Table 4. The relative errors of mean values are calculated, and the maximum relative errors are given as well. It can be found that the relative errors of mean values are both under 10%, which is acceptable for the validation of CFD modeling. Nevertheless, the maximum relative errors using the VOF model reach 12.71%, which exceeds 10%. Thus, compared to the VOF model, applying the Mixture model may obtain more reasonable results in the modeling of the OSBF.

Table 4 Comparison of air penetration depth

Parameter	Value	Source
Calculation/mm	86.86	Ref. [21]
Mean/mm	94.21	VOF
Error avg./%	8.46	VOF
Error max./%	12.71	VOF
Mean/mm	92.73	Mixture
Error avg./%	6.76	Mixture
Error max./%	7.61	Mixture

3.1.3 Flow characteristics in gas−slag system

The volume-weighted mean velocity of melt space is computed as well, as shown in Fig. 8. It can be found that the mean velocity fluctuates significantly within the time duration of 0−2 s, and then it gradually stabilizes at 0.351 m/s from 2 to 5 s. Although small fluctuations still exist, the gas−slag two-phase flow is regarded to reach a relatively stable state. Therefore, the results after 2 s are used for further analysis.

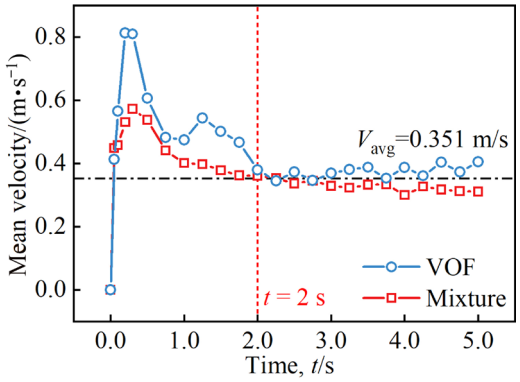

Fig. 8 Trend of mean velocity with time in slag area

To compare the gas−slag flow pattern in the bath, the contours of the air volume fraction (α) and vector distributions are shown in Figs. 9(a, b), respectvely. The isolines obtained by different models are extracted, as shown in Figs. 9(c, d). It should be noted that the isolines are extracted when the air volume fraction α=0.2, because the result under this criterion fits the experiment better [43]. Moreover, results without thermal expansion (TE) effects are marked with monochrome symbols as comparisons. Apparently, the airflow pattern in the industrial OSBF differs from that in the gas−water system, especially when using the VOF model. The most important difference is that the airflow moves

backward and attaches to the wall after leaving the nozzle in Figs. 9(b, d). However, this phenomenon is not obvious in Figs. 9(a, c), especially when ignoring the thermal expansion. Because of the thin layer of the melt between the lining and airflow, the airflow does not directly attach to the side wall. If the high-rate oxygen air moves backward and attaches to the wall in such a high-temperature bath, it may lead to severe erosion around the nozzles [35]. Commonly, the nozzles and firebricks can be protected by freezing accretion [24] when the airflow trajectory is similar to the outlines in Fig. 10(a). However, when the airflow trajectory changes into the state in Fig. 10(b), the nozzles or even the linings will be eroded. This could happen when the airflow keeps at a low rate. The photos of intact and eroded nozzles after using in practice are given in Fig. 10, and the operating parameters are in line with the numerical works. Therefore, the result obtained by the Mixture model is more reasonable because the thin layer still exists. This can be attributed to the "slip velocity" that makes the airflow reserve more momentum in the horizontal direction.

In summary, a complete numerical model considering thermal expansion is established, which has been validated with different theoretical and experimental results, such as the airflow trajectory, half-value radius, air penetration depth, and practical nozzles. After introducing the thermal effect on air density, this Mixture model involved with slip velocity can be better to obtain reasonable numerical results of OSBF.

3.2 Influences of operating and structure parameters on airflow

The backward motion of airflow in a high-temperature bath can cause nozzle erosion and severe accidents during production. Examinations of the flow patterns and thin layers under different factors are of great significance. In this part, the influences of airflow rates and furnace widths on

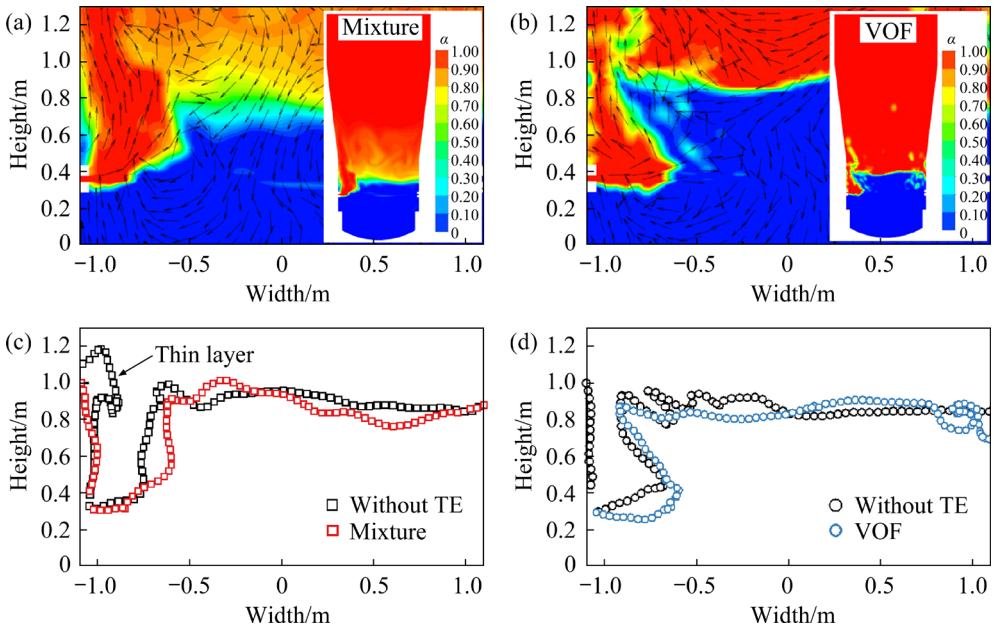

Fig. 9 Flow pattern in gas−slag system: (a, b) Contours and vectors; (c, d) Flow patterns

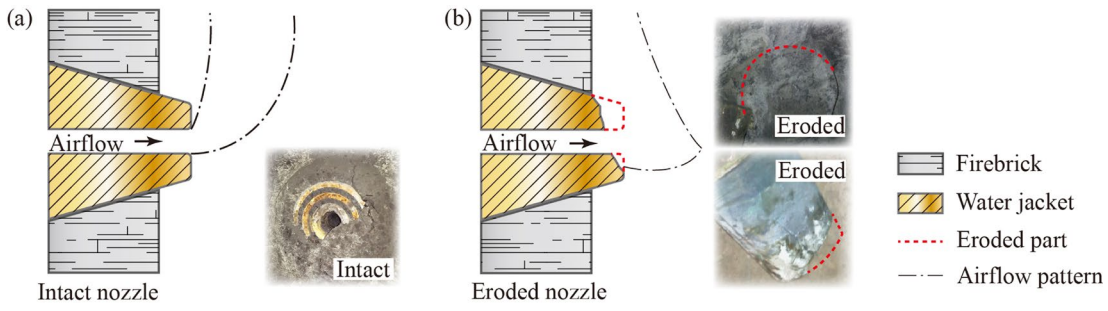

Fig. 10 Nozzles in industrial production: (a) Intact nozzle; (b) Eroded nozzle

airflow motion are analyzed. The reference condition is 225 m/s injection velocity and 2.2 m furnace width, which has been investigated in Section 3.1.3. The parameters of control groups are given in Table 2. Through comparison, it is not only to ensure production safety under common operating parameters but also to provide guidance on OSBF design.

3.2.1 Influence of airflow rate

The flow rate of air injection is one of the important operating parameters to control production, and it is also the critical factor that directly influences airflow patterns. Thus, three airflow rates that represent the common range of the operating parameter are investigated. The airflow injection velocities are 175, 225 and 275 m/s, respectively, and the corresponding mass flow rates can be found in Table 2. The isolines under different air velocities are extracted from Figs. 11(a, c, e) and shown in Figs. 11(b, d, f). The height (H) and width (W) of the furnace are normalized into dimensionless H_d and W_d, respectively, by dividing the nozzle diameter (d_0).

From Fig. 11, when compared with the result of 225 m/s, the airflow shrinks no matter the injection velocity increases or decreases. When the injection velocity decreases to 175 m/s, the inertia force of airflow will be counteracted by drag force soon, so the airflow will be dominated by buoyancy and flow upward. The backward motion of airflow is more obvious when injection velocity decreases. However, the airflow does not attach to the wall, and the thin layer between the wall and airflow seems to grow larger in the condition of 175 m/s.

In the condition of 275 m/s, the airflow shows high shrinkage at the height of 0.6−0.8 m. This can be caused by the violent melt fluctuation. On

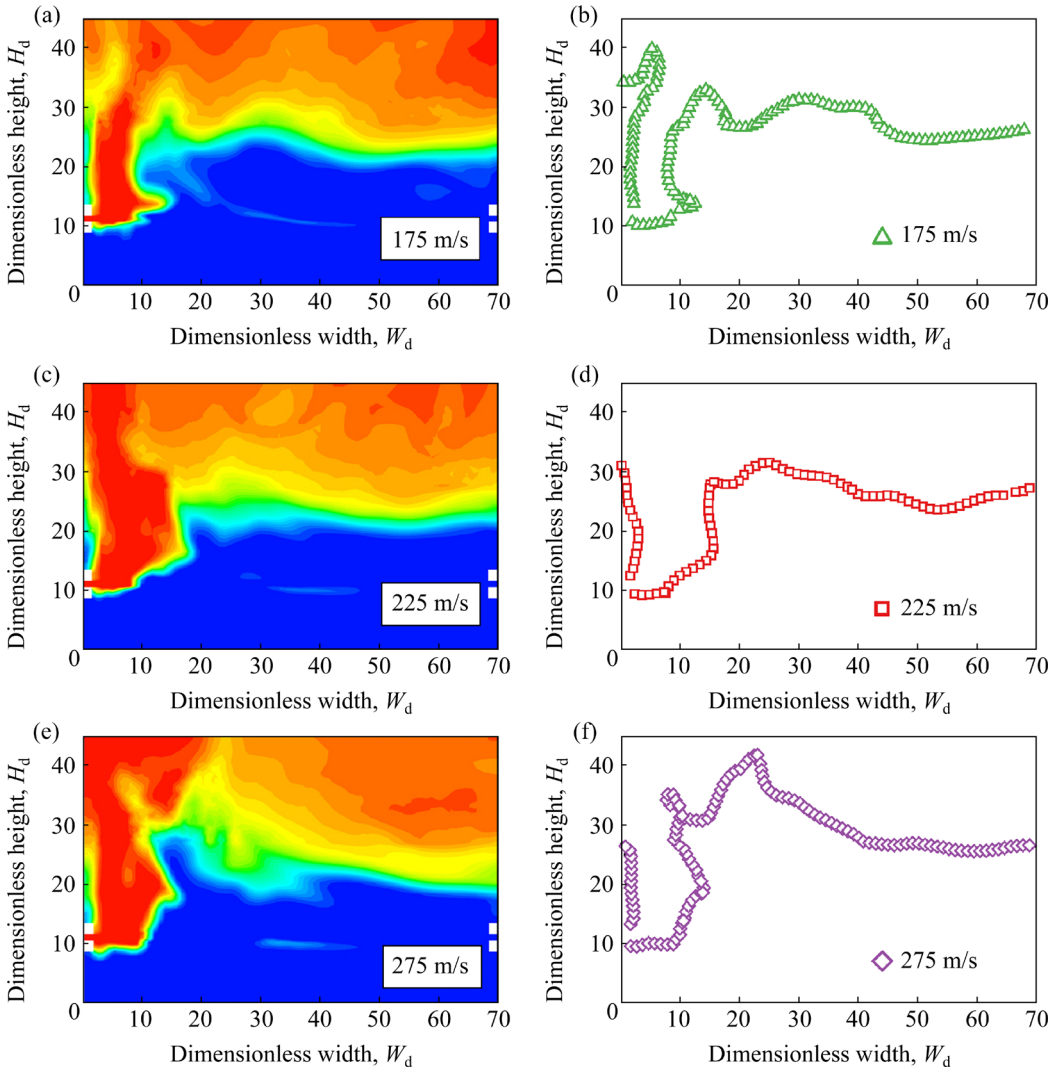

Fig. 11 Flow patterns with contours (a, c, e) and isolines (b, d, f) with different air velocities

the one hand, a higher velocity of airflow carried with higher momentum which would lead to more violent agitation of the melt phase. On the other hand, higher velocity injected more air volume per second, and its expansion would create a higher fluctuation. This intensive fluctuation forces the airflow near the free surface to attach to the wall, thus leading to the reduction of a thin layer.

To deeply analyze the thin layer, the isolines are enlarged to make a comparison, as shown in Fig. 12(a). It can be found that the height of the thin layer increases with the decline of air velocity, while the width varies in the range of 1−3d_0. Increasing air injection velocity brings more air volume and momentum per second, making the agitation more violent. The larger airflow expansion and higher melt fluctuation also lead to the reduction of the thin layer, especially for its height. This means that the airflow may still directly attach to the wall when the injection velocity exceeds 275 m/s. Meanwhile, decreasing injection velocity is not a foolproof measure to avoid the "attaching phenomenon", because the low-speed airflow may be squeezed directly to the wall.

The reduction of the thin layer can be reflected from the height and the area, and both of them are defined in Fig. 12(b). Figure 13 shows the areas and dimensionless heights of the thin layer under three conditions. It can be found that both the area and dimensionless height show a downward trend with the increase in air injection velocity. Based on this downward trend, the thin layer may disappear when the injection velocity increases to a certain extent. The shrinkage of a thin layer could be dangerous as the nozzle and lining could be eroded, but production safety could be guaranteed when the injection velocity is in the range of 175−275 m/s.

3.2.2 Influence of furnace widths

Due to the unique design of OSBF, it is convenient to increase the furnace length to meet the

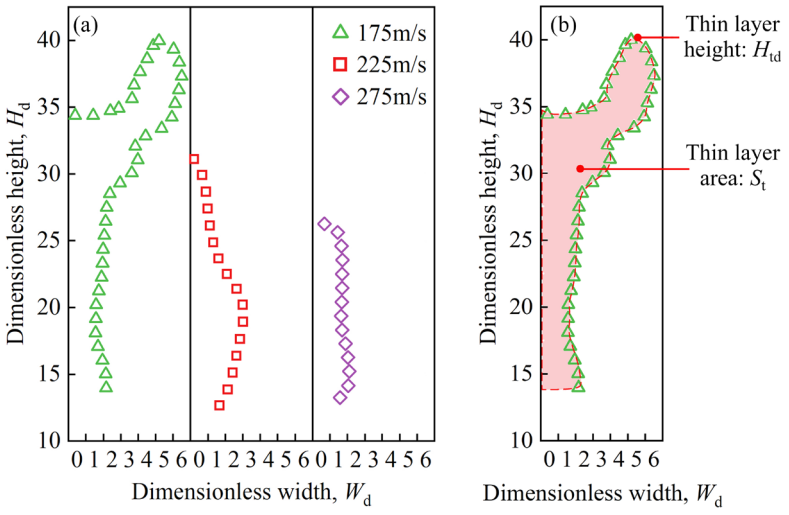

Fig. 12 Thin layers with different air velocities (a) and definition (b) of its height and area

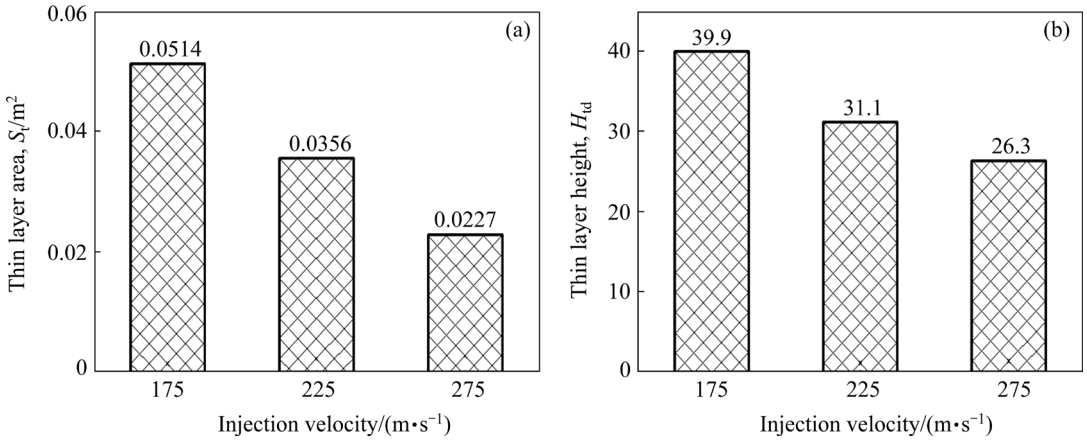

Fig. 13 Areas (a) and heights (b) of thin layers with different air velocities

higher capacity need. However, an excessively long furnace may result in difficulty in the tapping process. Thus, adding the furnace width for a larger production capacity is urgent, and the influence of furnace width on production safety should be analyzed. The furnace widths investigated in this study include 2.2, 2.5, and 2.8 m, but the injection velocities are all 225 m/s. The contours and isolines under different furnace widths are shown in Fig. 14. It can be found that the curves of three thin layers are similar, which are about $3d_0$ width at the height of $13-23d_0$ and $1d_0$ width at the height of $23-31d_0$. Also, the heights of the thin layers vary in a small range.

The areas and heights of thin layers under different furnace widths are given in Fig. 15. It can

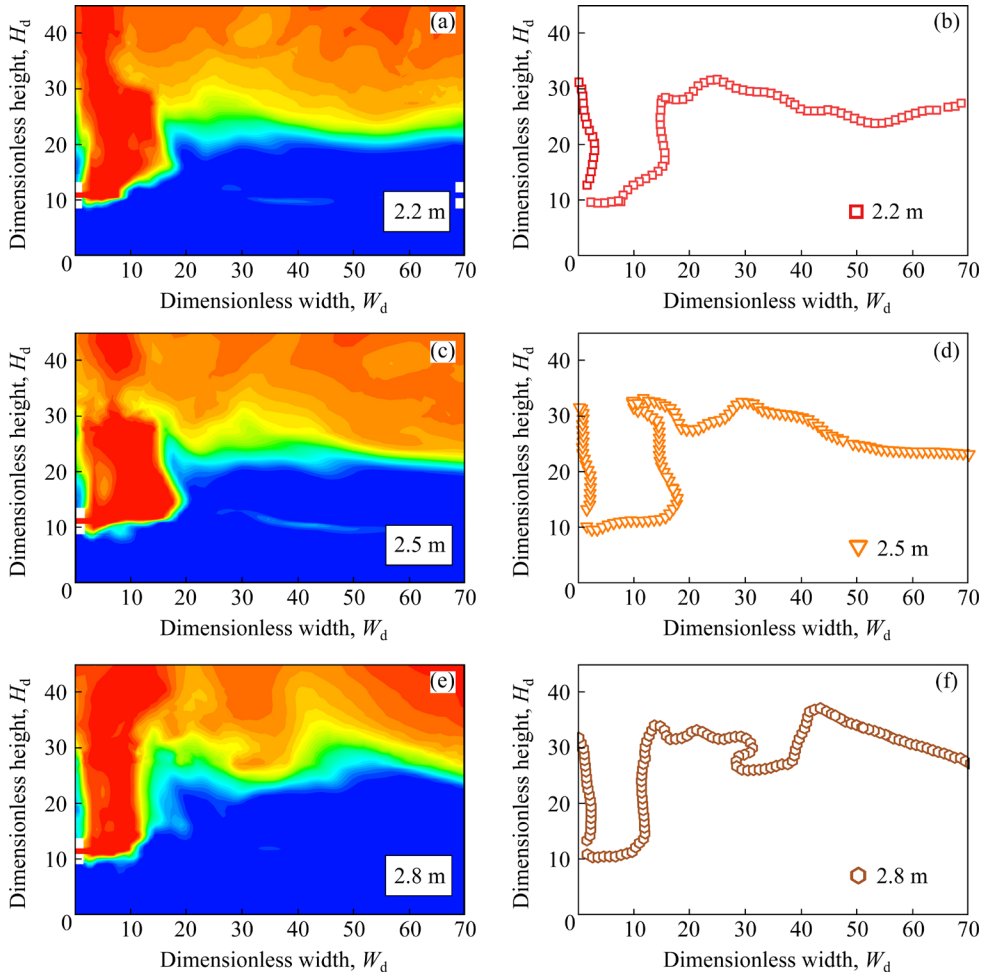

Fig. 14 Flow patterns with contours (a, c, e) and isolines (b, d, f) with different furnace widths

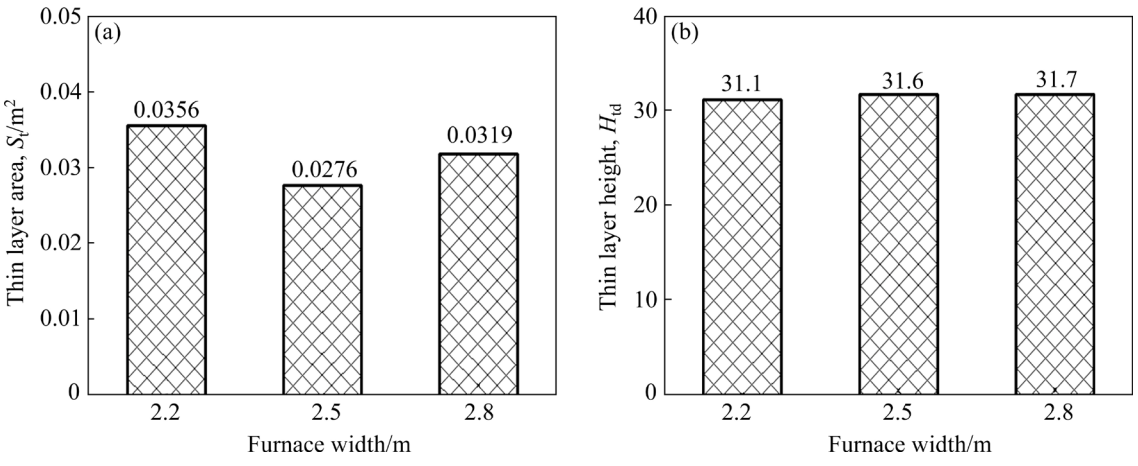

Fig. 15 Areas (a) and heights (b) of thin layers with different furnace widths

be found that the results of the three conditions are similar, and the results fluctuate with the increase in furnace width. The reason should be attributed to the maintenance of air injection velocity and nozzle submerged depth. On the one hand, the same injection velocity produces the same momentum and guarantees similar results in the airflow pattern. On the other hand, the same nozzle submerged depth shares the same static pressure that influences the airflow consistently. Therefore, the increase in furnace width shows a limited effect on the backward motion of airflow, which indicates that it could be a potential scheme for increasing the capacity.

4 Conclusions

(1) The Mixture model facilitated with slip velocity and gas thermal expansion effect is established. By comparing the numerical results with theoretical correlations of the airflow trajectory, half-value radius, and air penetration depth, this model is considered to obtain a more accurate simulation of the gas−liquid flow phenomenon in the OSBF.

(2) The flow pattern under a high-temperature bath is analyzed and demonstrates its possibility from the practice. A thin layer between the wall and airflow is found and considered to protect the lining from the erosion of high-rate oxygen airflows. Moreover, the thermal expansion effect of the gaseous phase significantly influences the gas−liquid flow pattern in the OSBF and may lead to severe backward motion of airflow. This could be a potential risk to production safety.

(3) With the increase in the air injection velocity, the thin layer between the wall and airflow shrinks. However, as the thin layer still exists, production safety can be guaranteed when the air injection velocity ranges from 175 to 275 m/s. On the other hand, as the thin layer shows small difference in the isoline pattern and height, the influence of furnace width on production safety is limited when the furnace width ranges from 2.2 to 2.8 m.

CRediT authorship contribution statement

Zhen-yu ZHU: Methodology, Software, Writing − Original draft preparation; **Ping ZHOU:** Project administration; **Xing-bang WAN:** Data curation, Validation; **Zhuo CHEN:** Methodology, Supervision; **Ling ZHANG:** Resources, Funding acquisition; **Shi-bo KUANG:** Conceptualization, Supervision, Writing − Reviewing and editing.

Declaration of competing interest

The authors declare that they have no known competing financial interests or personal relationships that could have appeared to influence the work reported in this paper.

Acknowledgments

The authors are grateful for the support from the National Key R&D Program of China (No. 2018YFC1901606). We also appreciate the High-performance Computing Center of Central South University (China) for assistance with the computations.

References

[1] LIU Zhi-hong, XIA Long-gong. The practice of copper matte converting in China [J]. Mineral Processing and Extractive Metallurgy, 2019, 128(1/2): 117−124. (DOI: 10.1080/25726641.2018.1543147)

[2] TASKINEN P, JOKILAAKSO A. Reaction sequences in flash smelting and converting furnaces: An in-depth view [J]. Metallurgical and Materials Transactions B, 2021, 52(5): 3524−3542. (DOI: 10.1007/s11663-021- 02283-7)

[3] SHI Jun-jie, PENG Chao, CHEN Min, LI Yun, ERIC H, KLEMETTINEN L, LUNDSTRÖM M, TASKINEN P, JOKILAAKSO A. Sulfation roasting mechanism for spent lithium-ion battery metal oxides under SO_2−O_2−Ar atmosphere [J]. JOM, 2019, 71(12): 4473−4482. (DOI: 10.1007/s11837-019-03800-5)

[4] WAN Xing-bang, FELLMAN J, JOKILAAKSO A, KLEMETTINEN L, MARJAKOSKI M. Behavior of waste printed circuit board (WPCB) materials in the copper matte smelting process [J]. Metals, 2018, 8(11): 887. (DOI: 10.3390/met8110887)

[5] WAN Xing-bang, SHI Jun-jie, TASKINEN P, JOKILAAKSO A. Extraction of copper from copper-bearing materials by sulfation roasting with SO_2−O_2 gas [J]. JOM, 2020, 72(10): 3436−3446. (DOI: 10.1007/s11837-020-04300-7)

[6] WAN Xing-bang, TASKINEN P, SHI Jun-jie, JOKILAAKSO A. A potential industrial waste–waste co-treatment process of utilizing waste SO2 gas and residue heat to recover Co, Ni, and Cu from copper smelting slag [J]. Journal of Hazardous Materials, 2021, 414: 125541. (DOI: 10.1016/j.jhazmat.2021.125541)

[7] SONG Ke-zhou, JOKILAAKSO A. Transport phenomena in copper bath smelting and converting processes—A review of experimental and modeling studies [J]. Mineral Processing and Extractive Metallurgy Review, 2022, 43(1): 107−121. (DOI: 10.1080/08827508.2020.1806835)

[8] LIU Fan-han. Characteristics analysis of the side-blown gas jet mixing process [J]. Proceedings of the Institution of Mechanical Engineers, Part C: Journal of Mechanical Engineering Science, 2021, 235(20): 4838−4850. (DOI: 10.1177/0954406220962826)

[9] ZHANG H L, ZHOU C Q, BING W U, CHEN Y M. Numerical simulation of multiphase flow in a Vanyukov furnace [J]. Journal of the Southern African Institute of Mining and Metallurgy, 2015, 115(5): 457−463.

[10] ALMARAZ A, LÓPEZ C, ARELLANO I, BARRÓN M A, JARAMILLO D, REYES F, PLASCENCIA G. CFD modelling of fluid flow in a Peirce–Smith converter with more than one injection point [J]. Minerals Engineering, 2014, 56: 102−108. (DOI: 10.1016/j.mineng. 2013.11.001)

[11] CHIBWE D K, AKDOGAN G, TASKINEN P. Numerical investigation of combined top and lateral blowing in a Peirce-Smith converter [J]. Chemical Product and Process Modeling, 2013, 8(2): 119−127. (DOI: 10.1515/cppm-2013-0036)

[12] GONZALEZ J, REAL C, PALOMAR-PARDAVE M, HOYOS L, GUTIERREZ M, MIRANDA R. CFD simulation gas-liquid flow in a copper converter with bottom air injection [J]. International Journal of Chemical Reactor Engineering, 2008, 6(1): 1−20. (DOI: 10.2202/1542-6580.1716)

[13] ZHAO Hong-liang, ZHAO Xing, MU Liang-zhao, ZHANG Li-feng, YANG Li-qiang. Gas-liquid mass transfer and flow phenomena in a Peirce−Smith converter: A numerical model study [J]. International Journal of Minerals, Metallurgy, and Materials, 2019, 26(9): 1092−1104. (DOI: 10.1007/s12613-019-1831-8)

[14] HUDA N, NASER J, BROOKS G A, REUTER M A, MATUSEWICZ R W. Computational fluid dynamic modeling of zinc slag fuming process in top-submerged lance smelting furnace [J]. Metallurgical and Materials Transactions B, 2012, 43(1): 39−55. (DOI: 10.1007/s11663-011-9558-6)

[15] HUDA N. Computational fluid dynamic modelling of zinc slag fuming process [D]. Melbourne, Australia: Swinburne University of Technology, 2012.

[16] CASTILLEJOS A H, BRIMACOMBE J K. Measurement of physical characteristics of bubbles in gas−liquid plumes: Part II. Local properties of turbulent air−water plumes in vertically injected jets [J]. Metallurgical Transactions B, 1987, 18(4): 659−671. (DOI: 10.1007/BF02672882)

[17] ZHU Miao-yong, SAWADA I, IGUCHI M. Physical characteristics of a horizontally injected gas jet and turbulent flow in metallurgical vessels [J]. ISIJ International, 1998, 38(5): 411−420. (DOI: 10.2355/ isijinternational.38.411)

[18] LIU Yan-ting, YANG Tian-zu, CHEN Zhuo, ZHU Zhen-yu, ZHANG Ling, HUANG Qing. Experiment and numerical simulation of two-phase flow in oxygen enriched side-blown furnace [J]. Transactions of Nonferrous Metals Society of China, 2020, 30(1): 249−258. (DOI: 10.1016/S1003-6326(19)65196-4)

[19] XIAO Ya-dong, WANG Jie, LU Ting-ting, LIU Feng-qin, LV Chao, ZHAO Hong-liang. An experimental study on gas–liquid flow and mixing behavior in a copper side-blown smelting furnace [J]. Metallurgical and Materials Transactions B, 2023, 54(2): 756−764. (DOI: 10.1007/s11663-023-02723-6)

[20] THEMELIS J N. Gas-liquid momentum transfer in a copper converter [J]. Transactions of the Metallurgical Society of AIME, 1969, 245: 2425−2433.

[21] HOEFELE E O, BRIMACOMBE J K. Flow regimes in submerged gas injection [J]. Metallurgical Transactions B, 1979, 10(4): 631−648. (DOI: 10.1007/BF02662566)

[22] IRONS G A, GUTHRIE R I L. Bubbling behaviour in molten metals [J]. Canadian Metallurgical Quarterly, 1980, 19(4): 381−387. (DOI: 10.1179/cmq.1980. 19.4.381)

[23] BUSTOS A A, RICHARDS G G, GRAY N B, BRIMACOMBE J K. Injection phenomena in nonferrous processes [J]. Metallurgical Transactions B, 1984, 15(1): 77−89. (DOI: 10.1007/bf02661065)

[24] HUDA N, NASER J, BROOKS G A, REUTER M A, MATUSEWICZ R W. CFD modeling of swirl and nonswirl gas injections into liquid baths using top submerged lances [J]. Metallurgical and Materials Transactions B, 2010, 41(1): 35−50. (DOI: 10.1007/s11663-009-9316-1)

[25] HUDA N, NASER J, BROOKS G A, REUTER M A, MATUSEWICZ R W. Computational fluid dynamics (CFD) investigation of submerged combustion behavior in a tuyere blown slag-fuming furnace [J]. Metallurgical and Materials Transactions B, 2012, 43(5): 1054−1068. (DOI: 10.1007/s11663-012-9686-7)

[26] WANG Yan-nan, VANIERSCHOT M, CAO Ling-ling, CHENG Zhong-fu, BLANPAIN B, GUO Mu-xing. Hydrodynamics study of bubbly flow in a top-submerged lance vessel [J]. Chemical Engineering Science, 2018, 192: 1091−1104. (DOI: 10.1016/j.ces. 2018.08.045)

[27] ZHAO Hong-liang, LU Ting-ting, YIN Pan, MU Liang-zhao, LIU Feng-qin. An experimental and simulated study on gas-liquid flow and mixing behavior in an ISASMELT furnace [J]. Metals, 2019, 9(5): 565. (DOI: 10.3390/met9050565)

[28] OBISO D, AKASHI M, KRIEBITZSCH S, MEYER B, REUTER M, ECKERT S, RICHTER A. CFD modeling and experimental validation of top-submerged-lance gas injection in liquid metal [J]. Metallurgical and Materials Transactions B, 2020, 51(4): 1509−1525. (DOI: 10.1007/s11663-020-01864-2)

[29] OBISO D, REUTER M, RICHTER A. CFD investigation of rotational sloshing waves in a top-submerged-lance metal bath [J]. Metallurgical and Materials Transactions B, 2021, 52(4): 2386−2394. (DOI: 10.1007/ s11663-021-02182-x)

[30] OBISO D, REUTER M, RICHTER A. CFD investigations of bath dynamics in a pilot-scale TSL furnace [J]. Metallurgical and Materials Transactions B, 2021, 52(5): 3064−3077. (DOI: 10.1007/s11663-021-02233-3)

[31] KONG Zheng, ZHAO Kai, ZHANG Qiao-rong, SHI Yan, ZHEN Chang-liang, SHI Xue-feng, ZHANG Xiao-hua. Numerical simulation of bubble formation behavior in oxygen coal combustion melting and separating furnace [J]. Asia-Pacific Journal of Chemical Engineering, 2020, 15: e2464. (DOI: 10.1002/apj.2464)

[32] LU Ting-ting, XIAO Ya-dong, ZHOU Yu-gao, SU Qiu-qiong, WEI Tao, LIU Feng-qin, ZHAO Hong-liang. Numerical simulation of nozzle height on the effect of fluid flow in a Peirce–Smith converter [J]. JOM, 2021, 73(10): 2938−2945.

(DOI: 10.1007/s11837-021-04813-9)

[33] VALENCIA A, ROSALES-VERA M, ORELLANA C. Fluid dynamics in a teniente type copper converter model with one and two tuyeres [J]. Advances in Mechanical Engineering, 2013, 5: 902874. (DOI: 10.1155/2013/ 902874)

[34] LIU Fan-han. Numerical simulation of enhanced side-blown stirring process and evaluation on mixing effect in Vanyukov furnace [D]. Kunming: Kunming University of Science and Technology, 2016. (in Chinese)

[35] ORYALL G N, BRIMACOMBE J K. The physical behavior of a gas jet injected horizontally into liquid metal [J]. Metallurgical Transactions B, 1976, 7(3): 391−403. (DOI: 10.1007/BF02652710)

[36] KUANG Shi-bo, CHU Kai-wei, YU Ai-bing, VINCE A. Numerical study of liquid−gas−solid flow in classifying hydrocyclones: Effect of feed solids concentration [J]. Minerals Engineering, 2012, 31: 17−31. (DOI: 10.1016/j. mineng.2012.01.003)

[37] SCHILLER L. A drag coefficient correlation [J]. Zeit Ver Deutsch Ing, 1933, 77: 318−320.

[38] MANNINEN M, TAIVASSALO V, KALLIO S. On the mixture model for multiphase flow [R]. Espoo, Finland: Technical Research Centre of Finland, 1996.

[39] ZHU Zhen-yu, ZHOU Ping, CHEN Zhuo, LONG Peng, ZHANG Ling. Numerical simulation on effect of air injection on two-phase flow in oxygen-enriched side-blown furnace [J]. Journal of Central South University (Science and Technology), 2022, 53(2): 398−408. (in Chinese) (DOI: 10.11817/j.issn.1672-7207.2022.02.004)

[40] XIA Tao. Numerical simulation and optimization of multiphase flow in the reduction furnace of the liquid rich-lead slag [D]. Changsha: Central South University, 2014. (in Chinese)

[41] ZHU Miao-yong, ZHOU Hai-bin, CHEN Zhao-ping, HUANG Zong-ze. Behaviors of jet and fluid flow in aod converter for stainless steel refining [J]. Acta Metallurgica Sinica, 2006, 42(6): 653−656. (in Chinese) (DOI: 10.3321/ j.issn:0412-1961.2006.06.016)

[42] MA Ji, SONG Yan-po, ZHOU Ping, CHENG Wei, CHU Shi-gan. A mathematical approach to submerged horizontal buoyant jet trajectory and a criterion for jet flow patterns [J]. Experimental Thermal and Fluid Science, 2018, 92: 409−419. (DOI: 10.1016/j.expthermflusci.2017.11.011)

[43] ZHU Zhen-yu. Numerical research on the two-phase flow in the lead side-blown smelting bath [D]. Changsha: Central South University, 2020. (in Chinese)

富氧侧吹炼铅炉内气液两相流动特征的数值模拟

祝振宇[1]，周 萍[1]，万兴邦[1]，陈 卓[1]，张 岭[2]，Shi-bo KUANG[3]

1. 中南大学 能源科学与工程学院，长沙 410083；

2. 长沙有色冶金设计研究院有限公司，长沙 410019；

3. ARC Research Hub for Computational Particle Technology, Department of Chemical Engineering, Monash University, Clayton, VIC 3800, Australia

摘 要：建立并验证一种能够较好模拟富氧侧吹熔池熔炼炉中气−液两相流动行为的数值模型，该模型包含两相滑移速度及气体热膨胀效应。利用多个理论关联式和实验结果验证数值模拟结果的准确性，并结合生产实践中喷嘴的侵蚀状态进行分析。通过对比，证明气体的热膨胀效应对两相流动过程影响显著，且可能会导致气流出现后座现象并对生产安全造成潜在风险。为此，进一步分析气流喷吹速度和炉体宽度对气流行为的影响，为富氧侧吹炉的操作制度和结构设计提供指导。研究发现，气流喷吹速度的提升，会致使防止富氧气流蚀损喷嘴的薄层熔体逐渐减少，但气流速度在 175~275 m/s 时仍可以保证生产安全。此外，炉体宽度从 2.2 m 提升至 2.8 m 时，薄层熔体在形状和高度上的变化较小，其对生产的安全性影响有限。

关键词：多相流；气流水平喷吹；气流后座；气体热胀性；侧吹炉；铅冶炼

(Edited by Xiang-qun LI)